Particuology 115 (2026) 228–237

Contents lists available at ScienceDirect

Particuology

journal homepage: www.elsevier.com/locate/partic

Effect of rotational motion on inertial migration of a neutrally buoyant rigid sphere in circular Poiseuille flow

Weile Luo[a], Fengxian Fan[a,b,*]

[a] School of Energy and Power Engineering, University of Shanghai for Science and Technology, Shanghai, 200093, China
[b] Shanghai Key Laboratory of Multiphase Flow and Heat Transfer in Power Engineering, University of Shanghai for Science and Technology, Shanghai, 200093, China

HIGHLIGHTS

- Fully resolved CFD–DEM simulations reveal rotation effects on inertial migration.
- Suppressing rotation consistently shifts equilibrium position toward pipe centerline.
- Migration dynamics alteration due to rotation suppression depends on initial position.
- Non-rotating spheres remain in monotonic regime, unlike freely rotating spheres.
- Suppressing rotation increases entry length required for full inertial migration.

GRAPHICAL ABSTRACT

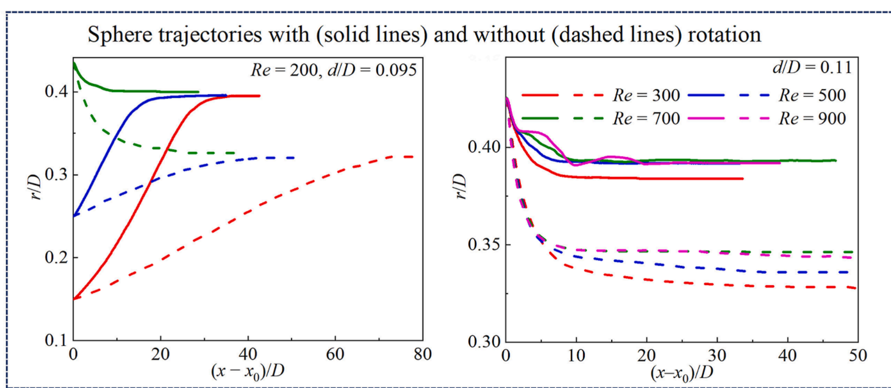

ARTICLE INFO

Keywords:
Particle-laden flow
CFD–DEM
Inertial migration
Microfluidics

ABSTRACT

Inertial migration of a neutrally buoyant rigid sphere in circular Poiseuille flow is strongly affected by particle rotation, yet its role remains poorly understood. This study employs three-dimensional fully-resolved CFD–DEM simulations to investigate inertial migration with and without particle rotation. The model is validated against experimental equilibrium radial positions. Simulation results reveal that suppressing rotation consistently shifts the equilibrium radial position toward the pipe centerline, but rotation's effect on the migration dynamics depends on the sphere's initial radial position. When rotation is suppressed, radial migration accelerates for the sphere released near the pipe wall, whereas radial migration slows for the sphere released closer to the centerline. While the freely rotating spheres experience a transition between different migration regimes as the sphere-to-pipe diameter ratio or the fluid Reynolds number increases, non-rotating spheres remain in the monotonic regime since they stabilize closer to the pipe centerline where both shear-gradient and wall-induced lift forces vanish. Moreover, suppressing rotation increases the entry length required for the sphere to achieve full migration. This study elucidates how particle rotation affects inertial migration and offers new insights into rotation-modulated lateral migration in microfluidics.

* Corresponding author. School of Energy and Power Engineering, University of Shanghai for Science and Technology, Shanghai, 200093, China.
E-mail address: fanfengxian@usst.edu.cn (F. Fan).

https://doi.org/10.1016/j.partic.2026.05.013
Received 12 February 2026; Received in revised form 24 April 2026; Accepted 12 May 2026
Available online 1 June 2026

1. Introduction

Inertial migration of neutrally buoyant rigid spheres within a circular pipe under Poiseuille flow condition not only represents a classical phenomenon in fluid mechanics but also serves as a fundamental principle for a variety of applications in microfluidics, such as particle focusing and separation (Anand and Subramanian, 2024; Bagi et al., 2024; Di Carlo et al., 2009). The inertial migration arises primarily from inertia and is affected by the confinement of pipe wall and the particle rotation (Bhagat et al., 2008; Alexeev et al., 2025), leading the spheres to converge at an equilibrium radial position between the pipe wall and the central axis. The prevailing explanation attributes this phenomenon to a competition between the shear-gradient lift force associated with the parabolic velocity profile in Poiseuille flow and the wall-induced lift force due to hydrodynamic asymmetry in the vicinity of pipe wall (Asmolov, 1999; Schonberg & Hinch, 1989; Zhang et al., 2020; Zhou & Papautsky, 2020).

Nevertheless, experimental observations have indicated that suppressing particle rotation shifts the equilibrium radial position closer to the pipe centerline compared with the freely rotating case (Oliver, 1962). In Oliver's experiments, rotation was suppressed by drilling a small off-center hole, which offset the center of gravity and generated a counteracting torque that hindered rotation. This design demonstrates that particle rotation can be effectively suppressed via mass asymmetry without significantly disturbing the flow field. Similar non-rotating behavior occurs for elongated particles in Poiseuille flow or shear flow, where they adopt stable, non-rotating orientations with vanishing net hydrodynamic torque (Einarsson et al., 2015; Karnis et al., 1966). External fields such as magnetic fields (Moerland et al., 2019) or electric fields (Riccardi & Martin, 2023) also offer non-invasive means to control particle rotation. Thus, the non-rotating condition, though idealized, is achievable—via mass asymmetry, external fields, or as a limiting case for non-spherical particles. Importantly, controlling particle rotation through these methods, even without complete suppression, can alter particle dynamics and thereby provide a technical route for effective particle manipulation in microfluidics. Yet, despite its potential for application, the mechanisms by which rotation affects inertial migration dynamics, as well as the extent of this influence, remain poorly understood.

Based on matched asymptotic theory, explicit relationships were developed between lift forces acting on a sphere and its radial position in a shear flow. These relationships have indicated that rotational effects are negligible, except under conditions of high shear and when the sphere is located near a wall (Saffman, 1965; Cherukat & McLaughlin, 1994; Ho & Leal, 1974). It is apparent that the matched asymptotic theory fails to explain the experimental results reported by Oliver (1962), which clearly showed that the equilibrium radial position is influenced by the particle rotation. The limitation of matched asymptotic theory may stem from its assumption that the particle Reynolds number, $Re_\mathrm{p} = Re(d/D)^2$, is much less than one—where Re is the fluid Reynolds number and d/D is the sphere-to-pipe diameter ratio. This assumption can restrict the theory's applicability to scenarios involving moderate Reynolds numbers and finite sphere sizes.

As numerical simulations become increasingly popular in the study of particle-laden flows, a number of numerical investigations have sought to elucidate the influence of particle rotation on inertial migration. Using the multi-particle collision dynamics method, Prohm et al. (2014) demonstrated that in two-dimensional Poiseuille flow with Reynolds numbers in the range from 6 to 33, a reduction in particle rotational velocity caused the equilibrium radial position to shift toward the channel centerline. Nevertheless, the mechanisms responsible for this behavior were not explored. Through lattice Boltzmann-discrete element methods, Liu and Wu (2021) investigated the dynamical process of a neutrally buoyant rigid sphere in two-dimensional Poiseuille flow with thermal convection, revealing that suppressing particle rotation significantly modified the inertial migration trajectory, yet without thorough analysis of how rotation alters the migration dynamics. Recently, Alexeev et al. (2025) conducted three-dimensional numerical simulations to assess the effect of particle rotation on the equilibrium radial position in Poiseuille flows. Nevertheless, they employed constrained simulations, where the sphere was confined to a prespecified radial location and its equilibrium radial position was determined by satisfying the zero-lift force condition. Consequently, the influence of particle rotation on the migration dynamics—including the trajectory and the axial entry length required to reach equilibrium—has not been determined.

Using a fully resolved two-way coupled CFD–DEM approach, we recently investigated the inertial migration dynamics of a freely rotating neutrally buoyant sphere in circular Poiseuille flow, characterizing its migration regime, radial equilibrium position and entry length, i.e., the axial distance required for the sphere to reach equilibrium (Luo et al., 2026). The results revealed that with increasing Reynolds number Re, the inertial migration behavior can be classified into three distinct regimes: (i) a monotonic regime, in which the sphere's radial position evolves monotonically toward the equilibrium; (ii) an overshooting regime, where the sphere overshoots the equilibrium only once before eventually relaxing to it; and (iii) an oscillation regime, characterized by damped oscillations about the equilibrium before finally stabilizing. These regimes were found to strongly influence how the equilibrium radial position and the entry length depend on the Reynolds number. It is important to note that Luo et al. (2026) focused exclusively on freely rotating spheres and did not examine the role of rotation in modulating the lift force components or net lift force governing particle migration dynamics.

As a follow-up to our previous work (Luo et al., 2026), the present study is specifically designed to elucidate the effect of particle rotation by systematically comparing freely rotating and non-rotating cases. We extend the numerical investigation to non-rotating spheres with the aim of providing mechanistic insight into how rotation influences inertial migration. The equilibrium radial positions in both freely rotating and non-rotating cases are validated through comparison with the experimental data from literature. A systematic comparison of migration dynamics under freely rotating and non-rotating conditions is conducted over a range of initial radial positions, sphere-to-pipe diameter ratios, and fluid Reynolds numbers. We elucidate how particle rotation affects the lift forces and determines the resultant migration behavior. Furthermore, we delineate the influence of rotation on both the final equilibrium radial position and the axial entry length required for full migration.

Although both the present study and that of Alexeev et al. (2025) focus on the effect of rotation on inertial migration, they differ significantly in methodological and scientific scope. Alexeev et al. (2025) employed dissipative particle dynamics simulations with lateral constraints to systematically quantify the force due to rotation, demonstrated its linear dependence on angular velocity, and proposed a corresponding scaling law. In contrast, the present study adopts a fully resolved three-dimensional CFD–DEM approach, in which a sphere migrates under the hydrodynamic force. This enables direct capture of the migration dynamics, including monotonic, overshooting, and oscillatory behaviors, as well as the entry length. Furthermore, we extend the parameter range to higher Reynolds numbers and smaller sphere-to-pipe diameter ratios to assess the feasibility of using rotation suppression for inertial migration control over a wider parameter space, and we examine how rotation affects the interplay among different lift force components during the inertial migration. These differences provide a complementary perspective on the role of particle rotation in inertial migration dynamics. Overall, the present study deepens the fundamental understanding of rotational effects on particle migration behavior in confined particulate flows and provides critical insights for the design of advanced particle manipulation technologies.

2. Model and method

This study investigates the inertial migration of a neutrally buoyant rigid sphere in a circular Poiseuille flow for both freely rotating and non-rotating cases. The computational setup used in the simulation is shown in Fig. 1. The fluid is assumed to be incompressible and Newtonian with a density ρ and a kinematic viscosity ν. The pipe has a diameter D and a length L. Unless otherwise specified, the simulations use $\rho = 1050$ kg/m^3, $\nu = 1.4286 \times 10^{-6}$ m^2/s, $D = 8$ mm, and $L = 2$ m. Our results confirm that $L = 2$ m is sufficiently long to allow the sphere to achieve full inertial migration. A fully developed parabolic velocity profile,

$$u(r) = u_{\max}\left[1 - \left(\frac{2r}{D}\right)^2\right] \tag{1}$$

is applied at the inlet, where $u(r)$ is the axial velocity at radial position r relative to the pipe centerline and $u_{\max}$ is the velocity at the centerline. A zero-pressure boundary condition is specified at the outlet, and a no-slip velocity condition is imposed at the solid boundaries, including both the pipe wall and the sphere surface. Initially, the sphere is positioned at a radial distance r_0 from the pipe centerline and an axial distance $x_0 = 4d$ from the pipe inlet. Its initial velocity $\boldsymbol{u}_{\mathrm{p}0}$ is set equal to the undisturbed fluid velocity at the particle center, meaning $\boldsymbol{u}_{\mathrm{p}0}$ is axially oriented with a magnitude of $u(r_0)$, as expressed by Eq. (1).

The simulations are carried out using a direct numerical simulation framework that couples the computational fluid dynamics (CFD) with the discrete element method (DEM), implemented on the open-source CFDEMcoupling platform (Kloss et al., 2012). Fluid-particle interactions are resolved using the fictitious domain method (FDM), in which the information on the rigid sphere motion—obtained from the DEM—is incorporated into the CFD as a body force term. To enable the accurate computation of fluid-solid interaction forces and torques at a reasonable computational cost, an adaptive mesh refinement strategy is employed in the numerical simulations. In such cases, the initial mesh elements occupied by the solid (particle) region undergo dynamic refinement and revert to their original state once the particle departs (Luo et al., 2026; Ren et al., 2023; Xia et al., 2020).

The fluid dynamics are governed by the incompressible Navier-Stokes equations, while the particle's translational and rotational motions follow Newton's second law. In the present FDM framework, the force $\boldsymbol{F}_{\text{f-p}}$ and torque $\boldsymbol{T}_{\text{f-p}}$ due to fluid-solid interaction can be expressed as

$$\boldsymbol{F}_{\mathrm{f-p}} = \int_{\Omega_s} \left(\rho\nu\nabla^2\boldsymbol{u} - \nabla p\right)\mathrm{d}\Omega_{\mathrm{s}} \tag{2}$$

$$\boldsymbol{T}_{\mathrm{f-p}} = \int_{\Omega_s} \left(\boldsymbol{r} - \boldsymbol{r}_{\mathrm{p}}\right) \times \left(\rho\nu\nabla^2\boldsymbol{u} - \nabla p\right)\mathrm{d}\Omega_{\mathrm{s}} \tag{3}$$

where $\boldsymbol{u}$ is the fluid velocity vector, p is the pressure, $\boldsymbol{r}$ is the position vector, and $\boldsymbol{r}_{\mathrm{p}}$ is the position vector of the particle's centroid. Moreover, Ω_{s} denotes the solid (particle) region.

To assess the influence of particle rotation on inertial migration, two scenarios are compared: the freely rotating case and the non-rotating case. In the former scenario, both translational and rotational motions are taken into account; while in the latter, particle rotation is suppressed by omitting the torque term given by Eq. (3) in the particle motion equations.

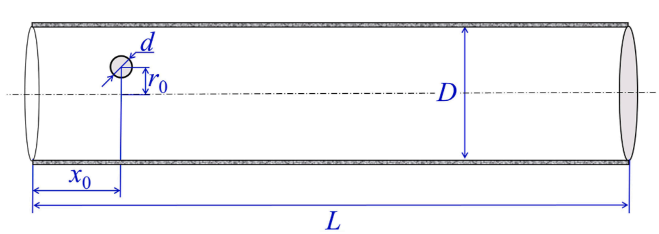

Fig. 1. Schematic of the computational setup used to simulate the inertial migration of a neutrally buoyant sphere in circular Poiseuille flow for both freely rotating and non-rotating cases. The sphere with a diameter d is initially located at a radial position r_0 relative to the pipe centerline and an axial position $x_0 = 4d$ relative to the pipe inlet, while the pipe itself has an inner diameter D and a length L.

3. Model validation

In order to validate the model and method, we performed numerical simulations involving a freely rotating neutrally buoyant sphere of $d/D = 0.095$ released from a fixed initial position of $r_0/D = 0.25$ at different Reynolds numbers. Fig. 2 presents the migration trajectories of the sphere over the Reynolds number range of $75 \le Re \le 1040$. From this figure, the migration regime, the equilibrium radial position r^* and the entry length L_{p} can be identified. While the migration regime and equilibrium position are readily obtained, L_{p} is determined using the following quantitative criteria. For the monotonic regime, L_{p} is the axial distance from the initial position to the point where the radial position reaches 99% (outward migration) or 101% (inward migration) of the equilibrium value. For the overshooting regime, the same 99% or 101% criterion is applied during returning phase from the maximum radial displacement after overshoot. For the oscillatory regime, migration is considered complete when the relative deviation of the radial position between a peak–valley pair in one cycle drops below 1%, and L_{p} is taken as the axial distance from the initial position to the midpoint between the peak and valley.

It is observed from Fig. 2(a) that for Reynolds numbers up to 480, the sphere undergoes outward radial migration, ultimately reaching a stable equilibrium position—a behavior classified as the monotonic migration regime. Within this regime, the equilibrium radial position shifts toward the pipe wall, while the entry length tends to decrease, as the Reynolds number increases. Interestingly, it is also observed that at very low Reynolds numbers, namely, $Re \le 145$, a higher Re does not guarantee a shorter entry length. These phenomena can be explained by the improved entry length model (Luo et al., 2026) based on matched asymptotic theory (Asmolov, 1999; Matas et al., 2009). Derived from a force balance between the lateral inertial lift and the viscous drag acting on the sphere under the assumption of constant radial migration velocity, the model yields an expression for the entry length L_{p} via a definite integral from the initial to the equilibrium position. It explicitly relates L_{p} to flow Reynolds number and the radial migration distance, but is limited to qualitative predictions for the monotonic regime, as the overshooting and oscillatory regimes deviate significantly from the constant-velocity assumption. For $r^* \ge r_0$, L_{p} is given by (Luo et al., 2026)

$$\frac{L_{\mathrm{p}}}{D} = 24\pi C_{\mathrm{L}}{}^{-1}Re^{-1}\left(\frac{d}{D}\right)^{-3}\left[\frac{r^* - r_0}{D} - \frac{4\left(r^{*3} - r_0^3\right)}{3D^3}\right] \tag{4}$$

where C_{L} is the lift coefficient, and r^* is the equilibrium radial position.

Eq. (4) indicates that the entry length decreases with the Reynolds number Re and increases with the radial displacement from the initial position, r^*-r_0. At very low Reynolds numbers ($Re \le 145$), an increase in Re results in a higher value of r^*-r_0, which exerts a greater influence on the variation of L_{p}/D than the Reynolds number itself, leading to a longer entry length.

However, for Reynolds numbers ranging from 575 to 1040, the sphere exhibits an overshoot beyond its equilibrium radial position during outward migration, attaining a maximum radial displacement prior to stabilizing at the equilibrium position, as depicted in Fig. 2(b). This behavior is identified as the overshooting regime, wherein the equilibrium radial position remains largely invariant and the entry length displays negligible variation, highlighting the fundamentally

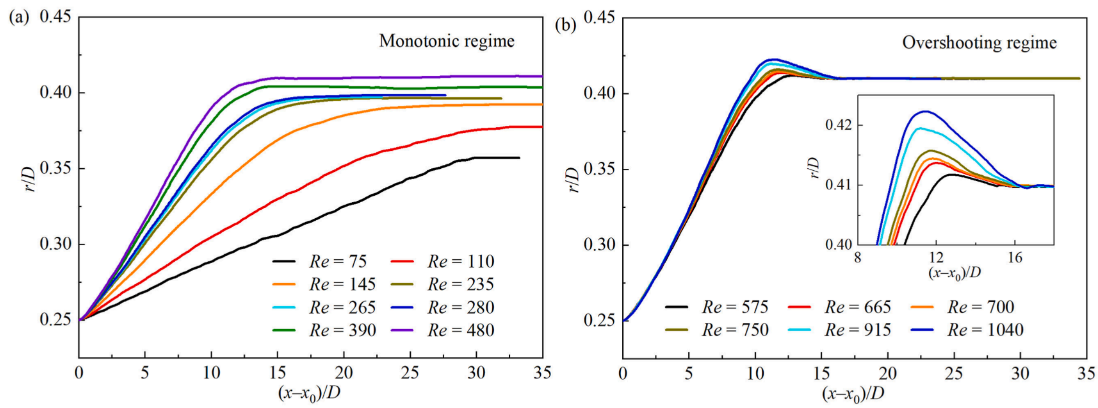

Fig. 2. Inertial migration trajectories of a freely rotating neutrally buoyant sphere ($d/D = 0.095$) released from an initial radial position $r_0/D = 0.25$ across various Reynolds numbers. (a) Monotonic regime for Re = 75–480; (b) Overshooting regime for Re = 575–1040. The inset in (b) shows an enlarged view of the region $0.4 \le r/D \le 0.425$ and $8 \le (x - x_0)/D \le 18$.

distinct nature of inertial migration dynamics compared to the monotonic regime. Moreover, overshooting presented here initiates at a Reynolds number of approximately 575, which falls between the critical Reynolds numbers of 800 and 500 associated with the onset of overshooting for $d/D = 0.083$ and 0.1, respectively, as reported in our previous study (Luo et al., 2026). This phenomenon further confirms that an increase in the sphere-to-pipe diameter ratio d/D lowers the critical Reynolds number separating adjacent migration regimes.

Fig. 3 compares the equilibrium radial positions obtained from numerical simulation results shown in Fig. 2 with the experimental data reported by Matas et al. (2004). The experiments were carried out in a pipe of inner diameter $D = 8$ mm, using spherical polystyrene beads of diameter $d = 0.76$ mm ($d/D = 0.095$) and density $\rho_p \approx 1050$ kg/m^3 at particle volume concentrations $\varphi < 0.01$ and a fluid of density matched that of the particles and kinematic viscosity calculated to be approximately 1.4286×10^{-6} m^2/s. The numerical results exhibit satisfactory agreement with experimental measurements under identical conditions of pipe diameter, particle characteristics, and fluid properties, with a maximum absolute relative deviation of 9.0% and a root mean square of the relative deviations of 3.6%. At relatively low Reynolds numbers ($Re \le 480$), the equilibrium radial position shifts progressively toward the pipe wall with increasing Re; however, as Re rises further, this position becomes saturated and independent of Re. This saturation behavior is also in qualitative accordance with the previous experimental observations for $Re = 100-1070$ at $d/D = 0.084$ (Morita et al., 2017). The relationship between the numerically determined equilibrium radial position and the Reynolds number can be well described by an exponential relaxation law:

$$\frac{r^*}{D} = \frac{r^*_\infty}{D}\left\{1 - \exp\left[-\left(\frac{Re}{Re_c} + \delta\right)\right]\right\} \tag{5}$$

where r^*_∞ is the asymptotic radial position, $r^*_\infty/D \approx 0.4095$, while the characteristic Reynolds number $Re_c \approx 107$ and the parameter $\delta \approx 1.44$ are obtained from a fit to the simulation data.

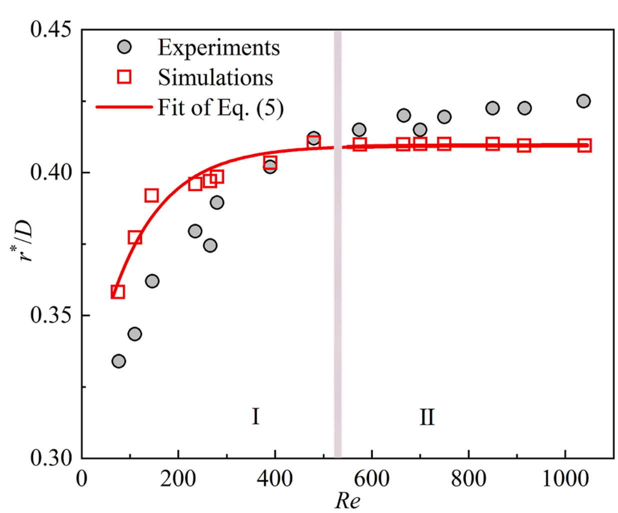

Fig. 3. Comparison between the numerically predicted equilibrium radial positions r^*/D and the experimental results of Matas et al. (2004) for a freely rotating neutrally buoyant sphere with $d/D = 0.095$ at the Reynolds numbers in the range of 75–1040. In the simulations, sphere's initial radial position was $r_0/D = 0.25$; however, the equilibrium radial position is independent of the initial position. Two different regimes are identified: a monotonic regime (I) for $Re \lesssim 480$, in which r^*/D increases with Re, and an overshooting regime (II) at higher Re, where r^*/D saturates at a value of 0.4095. The solid line shows a fit to the simulation data for both regimes.

To further validate the model and method, we performed simulations for both freely rotating and non-rotating cases under conditions matching the experiment of Oliver (1962): pipe diameter $D = 9.4$ mm, sphere-to-pipe diameter ratio $d/D = 0.245$, and fluid density $\rho = 1200$ kg/m^3. The fluid viscosity, though not directly reported in the experiment, is required for the simulations. We therefore determined an appropriate viscosity $\nu = 9.66 \times 10^{-7}$ m^2/s using the density-concentration-viscosity relations from literature (Jenkins & Marcus, 1995; National Research Council, 1928, 1929). In the experiments, the sphere was released either close to the pipe center or in contact with the pipe wall. The initial position was found to have little influence on the final equilibrium position, except for one run where the sphere released near the center ceased at $r/D = 0.035$, indicating negligible radial movement due to flow symmetry at the pipe centerline. We therefore excluded this data point from the comparison with our simulations. Fig. 4 compares the numerically predicted equilibrium radial positions with the experimental data of Oliver (1962). Our simulation results are in reasonable agreement with the experimental measurements for both freely rotating and non-rotating spheres. Both the simulations and experiments show that the equilibrium radial position varies with Reynolds number and shifts toward the pipe centerline when rotation is suppressed, thereby validating our simulation approach.

4. Results and discussion

4.1. Effect of particle rotation on inertial migration dynamics

To examine the inertial migration dynamics in the presence and absence of particle rotation, simulations were conducted for a sphere

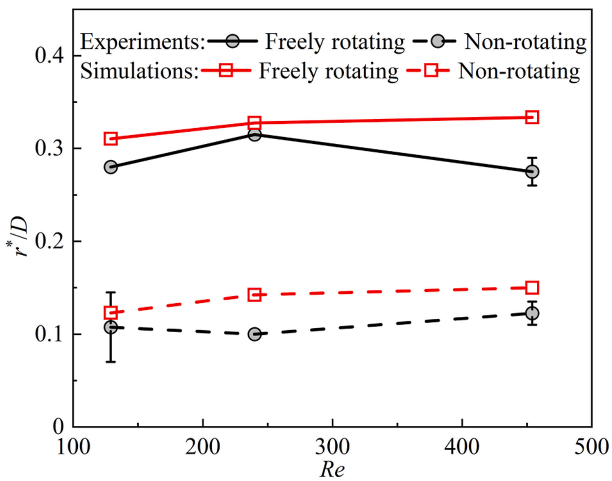

Fig. 4. Comparison between the numerically predicted equilibrium radial positions r^*/D and the experimental results of Oliver (1962) for freely rotating and non-rotating spheres with $d/D = 0.245$. In the simulations, the initial radial position was set to $r_0/D = 0.15$, while the equilibrium radial position is independent of the initial position. The experimental data are averaged from the two release positions (near the center and at the wall), except for the non-rotating case at $Re = 240$, where only the wall-release measurement is used because the center-released sphere showed negligible radial migration. Error bars represent the standard deviation of the two measurements.

located at different initial radial positions for two typical Reynolds numbers—$Re = 200$ and $Re = 700$—corresponding to the monotonic and overshooting regimes, respectively, for the freely rotating sphere (Fig. 2). Fig. 5 presents the inertial migration trajectories for four representative initial radial positions: two with $r_0 < r^*$, one with $r_0 = r^*$, and one with $r_0 > r^*$. The results indicate that for a given Reynolds number and rotational condition, the migration trajectory consistently converges to the same equilibrium radial position, independent of the initial radial position. Furthermore, under otherwise identical conditions, suppression of particle rotation consistently shifts the equilibrium position toward the pipe centerline, regardless of the migration regime. For instance, at $Re = 200$, the equilibrium radial position $r^*/D = 0.398$ for the freely rotating sphere but decreases to 0.324 when rotation is suppressed; at $Re = 700$, the corresponding positions are 0.410 and 0.349, respectively. This trend aligns with the experimental observations of Oliver (1962) and constrained dissipative particle dynamics simulations of Alexeev et al. (2025). In addition to reducing the equilibrium radial position r^*/D, suppression of particle rotation extends the entry length required for a sphere—starting from a given initial radial position, except at the equilibrium position—to attain equilibrium. When the initial position is $r_0/D = r^*/D$, the entry length becomes negligibly small. Moreover, as noted in previous experimental and numerical studies (Karnis et al., 1966; Aouane et al., 2022) on freely rotating spheres, the entry length exhibits a pronounced dependence on the initial radial position. For an initial radial position of $r_0/D = 0.25$, at $Re = 200$, the entry length L_p/D is 19.0 for a freely rotating sphere, compared to $L_p/D = 36.9$ when rotation is suppressed; at $Re = 700$, the corresponding values are 12.3 and 41.3, respectively. Similarly, at an initial radial position of $r_0/D = 0.435$ and $Re = 200$, $L_p/D = 7.0$ for the freely rotating case, compared to 22.3 with rotation suppressed; at $Re = 700$, the values are 3.8 and 13.0, respectively.

To gain a mechanistic insight into inertial migration, the lift forces exerted on the sphere and their influence on its trajectory are analyzed. Typically, four distinct lift forces arise from different mechanisms: the shear-gradient lift force F_{sg} due to curvature in the Poiseuille velocity profile, the wall-induced lift force F_w caused by flow asymmetry between the particle's near-wall and near-center sides, the slip-shear (Saffman) lift force F_{ss} resulting from the relative velocity between the particle and the fluid, and the Magnus lift force F_M associated with particle rotation. F_{sg} is directed toward the pipe wall, whereas the remaining lift forces act toward the pipe centerline.

Suppressing rotation eliminates F_M; however, previous theoretical and numerical studies have demonstrated that F_M is negligibly small compared to other lift forces. For instance, Saffman (1965) theoretically showed that for a freely rotating neutrally buoyant sphere, F_M is less by an order of magnitude than the shear-induced lift force when the particle Reynolds number is small. More recently, using dissipative particle dynamics simulations, Huang et al. (2020) concluded that F_M is one to two orders of magnitude smaller than F_{ss}, while the latter, together with F_w and F_{sg}, plays a critical role in determining the lateral equilibrium position for a ratio of sphere diameter to channel gap of 0.2 and $Re = 100$–500. Thus, the inward shift of the equilibrium position upon suppressing rotation arises from modifications of other lift components induced by rotation suppression, rather than simply from the elimination of F_M. Particularly, given that F_M is directed toward the pipe centerline, suppressing rotation eliminates this inward-directed force, and one might intuitively expect the equilibrium position to shift outward. However, our simulations, along with previous studies (Alexeev et al., 2025; Oliver, 1962), show an inward shift, implying that rotation suppression also affects other lift components, such as the shear-gradient and the wall-induced lift forces, thereby changing the overall force balance.

Based on the above analysis, a mechanistic understanding of how particle rotation affects inertial migration must focus on its influence on the shear-gradient lift force F_{sg}, the slip-shear lift force F_{ss}, as well as the

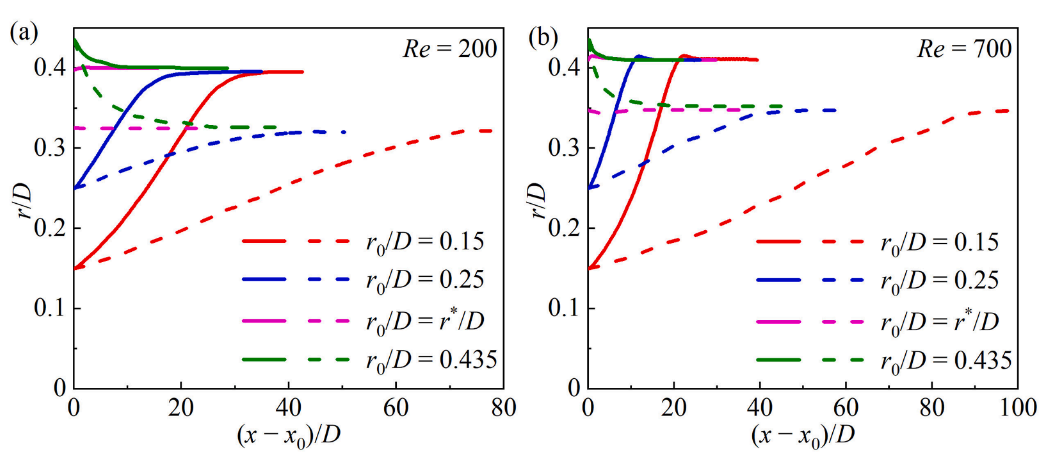

Fig. 5. Inertial migration trajectories of freely rotating (solid lines) and non-rotating (dashed lines) spheres released from different initial radial positions at $d/D = 0.095$: (a) $Re = 200$; (b) $Re = 700$.

wall-induced lift force F_w. Quantitative analysis of individual lift force components (F_{sg}, F_w, and F_{ss}) would provide a rigorous mechanistic explanation on the inertial migration dynamics of the non-rotating sphere compared to the freely rotating sphere. However, such decomposition is not feasible within the FDM framework used in the present study, where the fluid–particle interaction force is obtained by integrating hydrodynamic stresses over the particle region (Eq. (2)). Consequently, the force analysis presented here is qualitative and inferential, rather than a strict quantitative analysis.

Alexeev et al. (2025) have examined the effect of particle rotation on the shear-gradient lift force, demonstrating that suppressing rotation reduces the relative flow velocity on both the wall-faced and the center-faced sides of the sphere. This reduction weakens the shear-rate difference across the sphere, which in turn reduces the wall-directed shear-gradient lift force F_{sg} and shifts the equilibrium radial position inward (Alexeev et al., 2025). Nevertheless, the impact of rotation on the slip-shear and wall-induced lift forces, F_{ss} and F_w, remains an open question.

To clarify the role of particle rotation in the slip-shear lift force F_{ss}, the normalized slip velocity $(u_0 - u_{px})/u_{max}$ is compared between freely rotating and non-rotating spheres released from initial radial positions $r_0/D = 0.15$ and $r_0/D = 0.435$, as shown in Fig. 6. For particles released closer to the pipe centerline ($r_0/D = 0.15$), suppressing rotation has little effect on the slip velocity. In contrast, for particles released near the wall ($r_0/D = 0.435$), suppression of rotation leads to a pronounced decrease in the slip velocity. This decrease implies a reduction in the slip-shear lift force F_{ss}. Since F_{ss} acts toward the pipe centerline, its attenuation hinders the inward shift of the equilibrium position observed for non-rotating spheres.

To elucidate the role of particle rotation in the wall-induced lift force F_w, the Q-criterion of the flow is evaluated, where Q is defined as (Kovács & Balla, 2025)

$$Q = \frac{1}{2}\left(\|\boldsymbol{\Omega}\|^2 - \|\boldsymbol{S}\|^2\right) \tag{6}$$

where $\|\cdot\|$ denotes the Frobenius norm, while $\boldsymbol{\Omega}$ and $\boldsymbol{S}$ are the angular rotation rate tensor and the strain rate tensor, respectively. These tensors are computed from the velocity gradient tensor $\nabla \boldsymbol{u}$ as (Jeong & Hussain, 1995)

$$\boldsymbol{\Omega} = \frac{1}{2}\left[\nabla \boldsymbol{u} - (\nabla \boldsymbol{u})^{\mathrm{T}}\right] \tag{7}$$

$$\boldsymbol{S} = \frac{1}{2}\left[\nabla \boldsymbol{u} + (\nabla \boldsymbol{u})^{\mathrm{T}}\right] \tag{8}$$

Fig. 7 compares the Q-criterion fields for freely rotating and non-rotating spheres near two positions, namely $r/D = 0.176$ and $r/D = 0.413$. From a physical perspective, F_w originates from the interaction between the particle-induced disturbance flow and the nearby wall. The presence of the wall breaks the symmetry of this disturbance, leading to a transverse force, known as wall-induced lift force. This can be interpreted in terms of the far-field disturbance induced by the particle (Takemura & Magnaudet, 2003). At finite Reynolds numbers, this mechanism is closely related to the asymmetry of the wake structure: the wall breaks the symmetry of the wake vorticity distribution, resulting in an effective lift force acting on the particle (Zeng et al., 2005). The Q-criterion field provides a visualization of the vorticity structures. The enhanced asymmetry observed in the Q-criterion field reflects a strengthening of the wall-induced lift force F_w. While the Q-criterion field does not directly quantify F_w, its increased asymmetry is consistent with a stronger F_w. As can be seen from the figure, when rotation is suppressed, the Q-criterion fields exhibit enhanced flow asymmetry between the wall-faced and center-faced sides of the sphere, especially at $r_p/D = 0.413$, where the particle is closer to the wall. This increased asymmetry strengthens the wall-induced lift force F_w.

In summary, suppressing particle rotation alters the balance among the lift forces, shifting the equilibrium position closer to the pipe center. When a sphere is released near the pipe centerline, the shear-gradient lift force F_{sg} dominates and initially drives it outward. Particularly, under suppressed rotation, the magnitude of F_{sg} decreases, allowing the sphere to reach a final radial position closer to the centerline. In contrast, when a sphere is released near the pipe wall, the wall-induced lift force F_w dominates and drives it inward. Since F_w is enhanced without rotation, the sphere stabilizes at a radial position closer to the center. To enhance the understanding of lift forces during the inertial migration, the lift coefficients are estimated for freely rotating and non-rotating spheres, as detailed in Appendix Section A. These results provide robust qualitative evidence that particle rotation fundamentally modifies the balance of the lift forces of distinct mechanisms, thereby significantly affecting the equilibrium radial position of inertial migration.

The absence of particle rotation also alters the inertial migration regimes that characterize migration trajectory behaviors. When rotation is suppressed, a sphere released near the pipe centerline experiences a weaker outward lift force F_{sg}, leading to slower migration toward the pipe wall. Consequently, while a freely rotating sphere may enter an overshooting regime, a non-rotating sphere remains in a monotonic migration regime, as illustrated in Fig. 5(b). To elucidate the inertial migration regimes of freely rotating and non-rotating spheres, the transient lift forces (Eq. (A1) in Appendix Section A) for an initial position $r_0/D = 0.15$ at Reynolds numbers of 200 and 700 have been computed, as detailed in Appendix Section B. The results show that the sphere exhibits monotonic migration, primarily because both the lift force and the migration velocity remain small when the sphere first crosses the equilibrium radial position, regardless of rotation. Particularly, at a high Reynolds number ($Re = 700$), the non-rotating sphere remains in the monotonic regime because its equilibrium position lies closer to the pipe centerline, where the net lift force vanishes.

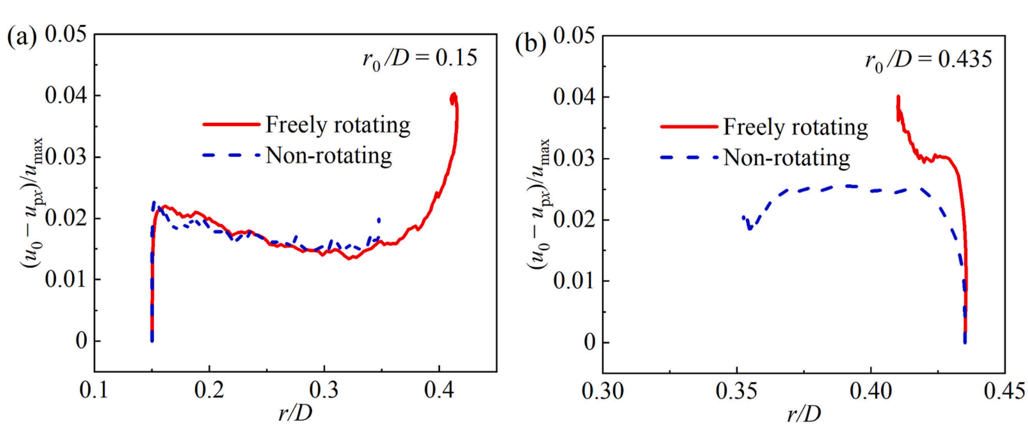

Fig. 6. Variation of the normalized slip velocity $(u_0 - u_{px})/u_{max}$ with radial position during the inertial migration for freely rotating and non-rotating spheres at $Re = 700$ and $d/D = 0.095$. Particles are released from two representative positions, corresponding to $r_0/D = 0.15$ (a) and $r_0/D = 0.435$ (b), located near the pipe centerline and near the pipe wall, respectively. Moreover, u_0 denotes the undisturbed fluid velocity at the particle center, while u_{px} denotes the axial velocity of the particle's translational motion, i.e., the particle velocity at its center.

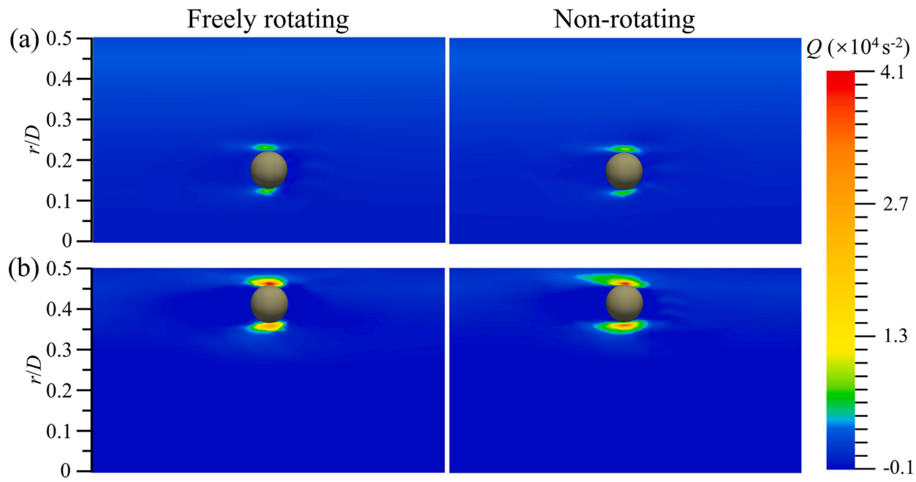

Fig. 7. Q-criterion fields in a longitudinal section through the sphere center for freely rotating and non-rotating cases at $Re = 700$ and $d/D = 0.095$. Results are presented for two distinct particle positions, corresponding to $r_p/D = 0.176$ (a) and $r_p/D = 0.413$ (b), located closer to the pipe center ($r/D = 0$) and near the pipe wall ($r/D = 0.5$), respectively.

To further understand why the entry length of a non-rotating sphere is longer than that of a freely rotating sphere, we plot the normalized radial position r/D as a function of the dimensionless time $t\nu/D^2$ for both cases in Fig. 8. Except for spheres initially located at the equilibrium position, the time required for a non-rotating sphere to reach equilibrium is longer than that for a freely rotating one. For spheres initially located near the centerline, the non-rotating sphere migrates radially more slowly and thus remains in the regions of higher axial velocities for a longer duration, resulting in a longer entry length for completing inertial migration. In contrast, for spheres initially located near the wall, the non-rotating sphere experiences a stronger inward-directed lift force F_w during the initial migration stage. This force, however, decays rapidly as the particle moves toward the pipe centerline. Consequently, the non-rotating sphere initially exhibits a faster radial migration compared to its freely rotating counterpart. Nevertheless, because its equilibrium radial position lies closer to the pipe centerline, it is subsequently carried by higher-velocity fluid in the axial direction, again requiring a longer entry length to complete inertial migration.

4.2. Influence of sphere-to-pipe diameter ratio

The effect of the sphere-to-pipe diameter ratio d/D on the inertial migration of freely rotating and non-rotating spheres was examined by varying d/D in the range from 0.083 to 0.167. Fig. 9 presents the inertial migration trajectories for various d/D values under freely rotating and non-rotating conditions at two representative Reynolds numbers, $Re = 200$ and $Re = 700$.

As shown in Fig. 9(a), at low inertia ($Re = 200$), both freely rotating and non-rotating spheres migrate monotonically toward their equilibrium radial positions for all tested d/D values, suggesting that the inertia is too weak to trigger overshooting or oscillatory motion, regardless of sphere rotation. For a given d/D, compared to the freely rotating sphere, the non-rotating sphere requires a greater entry length L_p/D to achieve equilibrium, since its equilibrium position is closer to the pipe centerline where the fluid axial velocity is higher, thereby extending the axial migration distance. Moreover, increasing d/D accelerates the radial migration of the sphere from the pipe wall toward the centerline, indicating stronger wall-induced lift forces on larger particles.

At a higher inertial condition ($Re = 700$, Fig. 9(b)), the influence of d/D on the inertial migration trajectory becomes more evident. The migration trajectory of freely rotating sphere transitions from monotonic regime to overshooting regime and eventually to oscillatory regime, as d/D increases. In contrast, non-rotating spheres maintain monotonic convergence across all d/D values examined. This behavior arises because suppressing rotation strengthens the wall-induced lift force, driving the sphere to migrate rapidly toward the near-center region, where both shear-gradient lift force F_{sg} and wall-induced lift force F_w diminish. As a result, radial migration becomes very slow in this region, allowing the sphere to reach and remain at the equilibrium radial position. This leads to monotonic convergence, even for a sphere

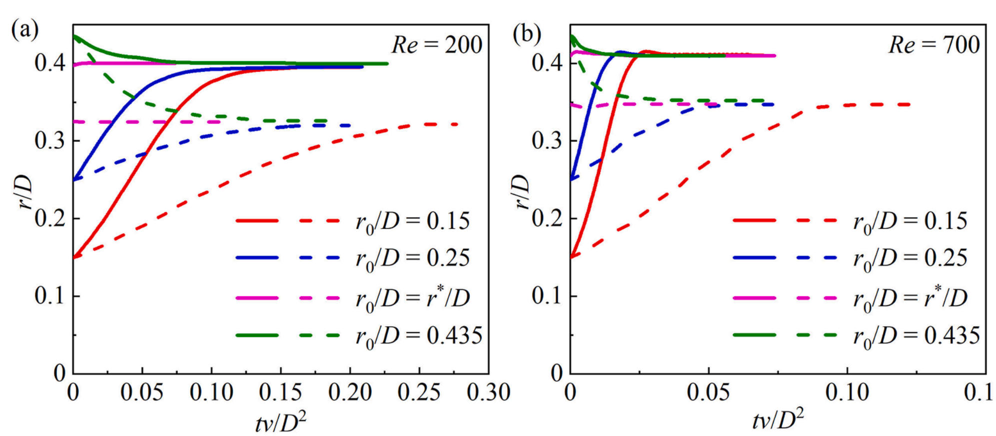

Fig. 8. Normalized radial position r/D as a function of the dimensionless time $t\nu/D^2$ for freely rotating (solid lines) and non-rotating (dashed lines) spheres released from different initial radial positions at $d/D = 0.095$: (a) $Re = 200$; (b) $Re = 700$.

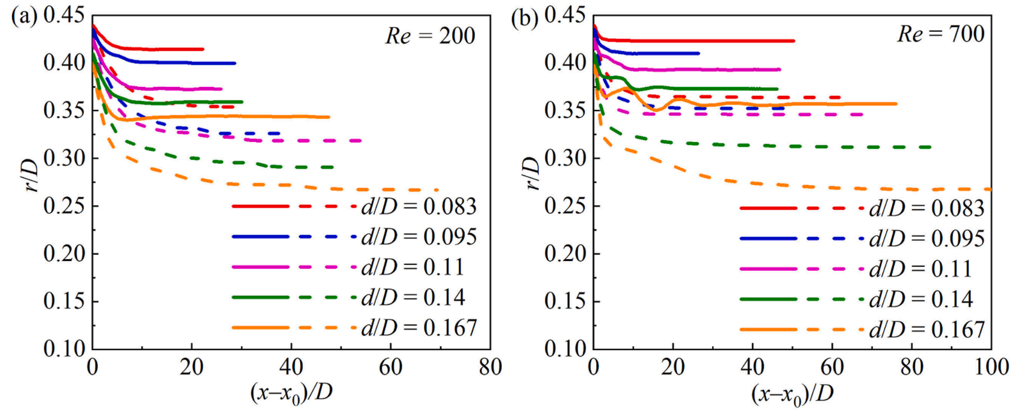

Fig. 9. Inertial migration trajectories for various sphere-to-pipe diameter ratios under freely rotating (solid lines) and non-rotating (dashed lines) conditions, at two representative Reynolds numbers: (a) $Re = 200$; (b) $Re = 700$. In the simulations, the spheres were released from an initial radial position near the pipe wall, with the gap (Δ) between the particle surface and the wall maintained at a fixed dimensionless separation of $\Delta/D = 0.02$.

as large as $d/D = 0.167$. To gain deeper mechanistic insight into the migration regimes, the net lift forces during inertial migration for freely rotating and non-rotating spheres at $d/D = 0.167$ and Reynolds numbers of 200 and 700 are provided in Appendix Section B. The results confirm that the non-rotating sphere remains in the monotonic regime, which is closely linked to its equilibrium position being located closer to the pipe centerline, where the net lift force is inherently weak.

Fig. 10 presents the normalized equilibrium radial position r^*/D as a function of the sphere-to-pipe diameter ratio d/D under freely rotating and non-rotating conditions at two representative Reynolds numbers, $Re = 200$ and $Re = 700$. It is observed that for freely rotating spheres, the equilibrium radial position r^*/D shifts toward the pipe centerline with increasing d/D, consistent with experimental observations by Matas et al. (2004). In contrast, although the non-rotating spheres exhibit a similar trend in r^*/D versus d/D, their r^*/D values are significantly smaller than those of the freely rotating case at the same d/D. This inward shift of equilibrium position at higher d/D indicates that wall-induced lift force F_w increases more rapidly than shear-gradient lift force F_{sg} with increasing sphere size.

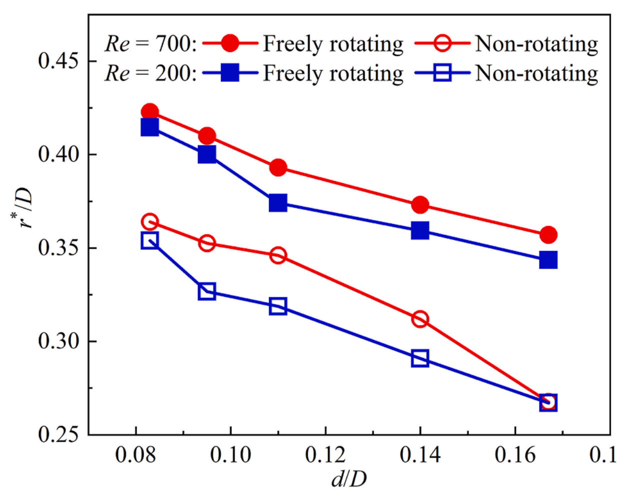

Fig. 10. Normalized equilibrium radial position r^*/D as a function of the sphere-to-pipe diameter ratio d/D under freely rotating and non-rotating conditions at two representative Reynolds numbers, $Re = 200$ and $Re = 700$. In the simulations, same dimensionless separation between the particle surface and the pipe wall Δ/D as in Fig. 9 was used.

4.3. Influence of fluid Reynolds number

Fig. 11 presents the inertial migration trajectories for various Reynolds numbers under freely rotating and non-rotating conditions at $d/D = 0.11$ and $r_0/D = 0.425$. For the freely rotating case, the inertial migration behavior varies with the Reynolds number. At a Reynolds number of $Re \le 700$, the sphere migrates monotonically toward the equilibrium radial position. When Re increases beyond 700, inertial effects become strong enough to induce a damped oscillatory migration around the equilibrium position. In contrast, the migration trajectory of the non-rotating sphere shows a distinctly different Reynolds number dependence. Throughout the examined Reynolds number range, only monotonic convergence is observed, even at $Re = 900$, because the equilibrium positions lie closer to the pipe centerline, where the net lift force is diminished. Furthermore, under the present simulation conditions, the entry length L_p/D ranges between 10 and 30 depending on Re, indicating rapid inertial migration for spheres released near the pipe wall.

Fig. 12 presents the normalized equilibrium radial position r^*/D as a function of the Reynolds number Re for freely rotating and non-rotating spheres. In both cases, r^*/D shifts toward the pipe wall and eventually saturates as the Reynolds number increases. However, the equilibrium radial positions of non-rotating spheres remain consistently closer to the pipe centerline than those of freely rotating particles, indicating that suppressing rotation promotes inward migration. The data for both freely rotating and non-rotating cases are well described by Eq. (5). For

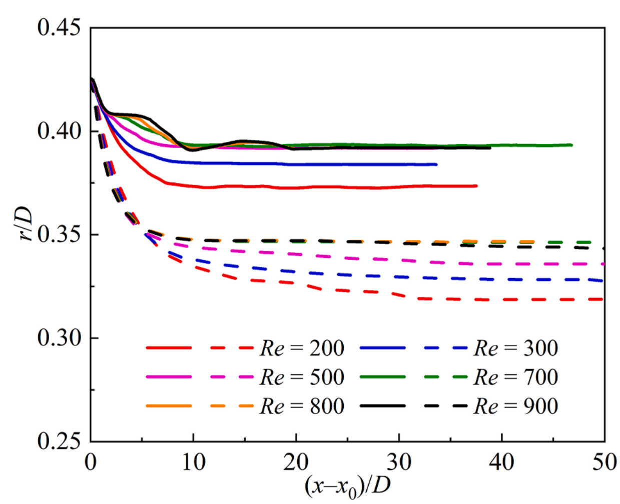

Fig. 11. Inertial migration trajectories for various Reynolds numbers under freely rotating (solid lines) and non-rotating (dashed lines) conditions. Simulations were performed using $d/D = 0.11$ and $r_0/D = 0.425$.

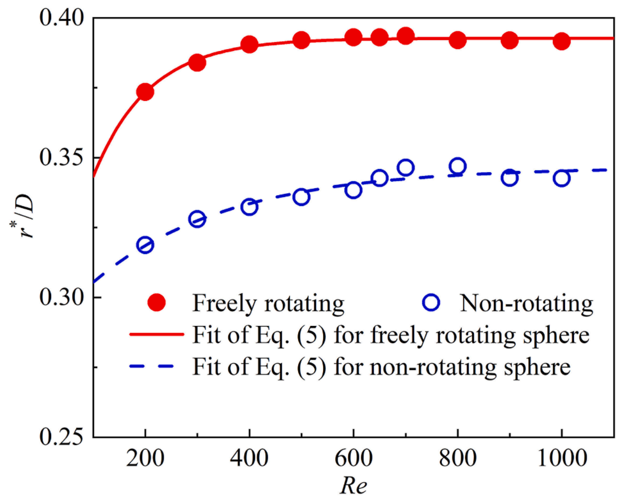

Fig. 12. Normalized equilibrium radial position r^*/D as a function of the Reynolds number Re for freely rotating and non-rotating spheres. Simulations were performed using $d/D = 0.11$ and $r_0/D = 0.425$. Solid and dashed lines represent fits to the simulation data for freely rotating and non-rotating spheres, respectively.

the freely rotating case, the asymptotic radial position $r^*_\infty/D \approx 0.395$, the characteristic Reynolds number $Re_c \approx 150$, and the parameter $\delta \approx 1.67$, whereas for the non-rotating case, $r^*_\infty/D \approx 0.3465$, $Re_c \approx 260$, and $\delta \approx 1.75$.

5. Conclusions

We performed three-dimensional fully-resolved CFD–DEM simulations to investigate the effect of particle rotation on the inertial migration of a neutrally buoyant rigid sphere in a fully developed circular Poiseuille flow. The equilibrium radial positions obtained numerically for both freely rotating and non-rotating spheres were validated against experimental data from the literature. On this basis, the influence of particle rotation on inertial migration dynamics—including the migration regime, equilibrium radial position, entry length, and the underlying lift forces—was clarified. Furthermore, the effects of sphere-to-pipe diameter ratio and the fluid Reynolds number were examined by varying the diameter ratio from 0.083 to 0.167 and the Reynolds number from 200 to 1000, under both freely rotating and non-rotating conditions.

Numerical simulations reveal that while suppressing particle rotation consistently shifts the equilibrium radial position toward the pipe centerline, the effect of rotation on migration dynamics is highly dependent on the sphere's initial radial position. Specifically, when rotation is suppressed, radial migration accelerates for spheres released near the pipe wall, whereas it decelerates for those released closer to the centerline. These phenomena arise from an enhanced inward wall-induced lift force and a reduced outward shear-gradient lift force in the absence of rotation.

Furthermore, as the sphere-to-pipe diameter ratio or fluid Reynolds number increases, freely rotating spheres transition from monotonic to overshooting and eventually to oscillatory migration regime. In contrast, suppressing particle rotation results solely in monotonic migration, as non-rotating spheres migrate toward an equilibrium position closer to the pipe centerline, where both wall-induced and shear-gradient lift forces become minimal. The entry length required for full inertial migration is also dependent on particle rotation. Suppressing rotation leads to an increase in the entry length, because non-rotating spheres reach equilibrium closer to the pipe centerline, where higher axial fluid velocities extend the axial displacement needed to complete migration.

This study not only elucidates the role of particle rotation in inertial migration dynamics but also provides new insights into how rotational effects modulate inertial migration. These findings can be applied to achieve particle focusing and separation via rotation-based modulation in inertial microfluidic systems. It is worth noting that the present study focuses on mechanistic insight rather than a general scaling framework. In future work, a reduced-order method capable of isolating individual lift components—for example, by examining the slip-shear lift under controlled surface slip conditions or the wall-induced lift in a linear shear flow—could be used to model the lift force and thereby provide a scaling law for inertial migration dynamics.

CRediT authorship contribution statement

Weile Luo: Writing – original draft, Methodology, Investigation, Formal analysis. **Fengxian Fan:** Writing – review & editing, Supervision, Resources, Methodology, Funding acquisition, Data curation, Conceptualization.

Declaration of competing interest

The authors declare that they have no known competing financial interests or personal relationships that could have appeared to influence the work reported in this paper.

Acknowledgments

The authors are grateful to the National Natural Science Foundation of China (Grant No. 52476157) for the financial support of this work. Support from High Performance Computing Center at University of Shanghai for Science and Technology is also greatly acknowledged.

Appendix A. Supplementary data

Supplementary data to this article can be found online at https://doi.org/10.1016/j.partic.2026.05.013.

References

Alexeev, D., Litvinov, S., Economides, A., Amoudruz, L., Toner, M., & Koumoutsakos, P. (2025). Inertial focusing of spherical particles: The effects of rotational motion. *Physical Review Fluids, 10*, Article 054202. https://doi.org/10.1103/PhysRevFluids.10.054202

Anand, P., & Subramanian, G. (2024). Inertial migration in a pressure-driven channel flow: Beyond the Segre-Silberberg pinch. *Physical Review Letters, 132*, Article 054002. https://doi.org/10.1103/PhysRevLett.132.054002

Aouane, O., Sega, M., Bäuerlein, B., Avila, K., & Harting, J. (2022). Inertial focusing of a dilute suspension in pipe flow. *Physics of Fluids, 34*, Article 113312. https://doi.org/10.1063/5.0111680

Asmolov, E. S. (1999). The inertial lift on a spherical particle in a plane Poiseuille flow at large channel Reynolds number. *Journal of Fluid Mechanics, 381*, 63–87. https://doi.org/10.1017/S0022112098003474

Bagi, M., Amjad, F., Ghoreishian, S. M., Shahsavari, S. S., Huh, Y. S., Moraveji, M. K., & Shimpalee, S. (2024). Advances in technical assessment of spiral inertial microfluidic devices toward bioparticle separation and profiling: A critical review. *Biochip Journal, 18*, 45–67. https://doi.org/10.1007/s13206-023-00131-1

Bhagat, A. A. S., Kuntaegowdanahalli, S. S., & Papautsky, I. (2008). Enhanced particle filtration in straight microchannels using shear-modulated inertial migration. *Physics of Fluids, 20*, Article 101702. https://doi.org/10.1063/1.2998844

Cherukat, P., & McLaughlin, J. B. (1994). The inertial lift on a rigid sphere in a linear shear flow field near a flat wall. *Journal of Fluid Mechanics, 263*, 1–18. https://doi.org/10.1017/S0022112094004015

Di Carlo, D., Edd, J. F., Humphry, K. J., Stone, H. A., & Toner, M. (2009). Particle segregation and dynamics in confined flows. *Physical Review Letters, 102*, Article 094503. https://doi.org/10.1103/PhysRevLett.102.094503

Einarsson, J., Candelier, F., Lundell, F., Angilella, J. R., & Mehlig, B. (2015). Rotation of a spheroid in a simple shear at small Reynolds number. *Physics of Fluids, 27*, Article 063301. https://doi.org/10.1063/1.4921543

Ho, B. P., & Leal, L. (1974). Inertial migration of rigid spheres in two-dimensional unidirectional flows. *Journal of Fluid Mechanics, 65*(2), 365–400. https://doi.org/10.1017/S0022112074001431

Huang, Y., Zhao, X., & Pan, Y. (2020). Slip-shear and inertial migration of finite-size spheres in plane Poiseuille flow. *Computational Materials Science, 176*, Article 109542. https://doi.org/10.1016/j.commatsci.2020.109542

Jenkins, H. D. B., & Marcus, Y. (1995). Viscosity B-coefficients of ions in solution. *Chemical Reviews, 95*(8), 2695–2724. https://doi.org/10.1021/cr00040a004

Jeong, J., & Hussain, F. (1995). On the identification of a vortex. *Journal of Fluid Mechanics, 285*, 69–94. https://doi.org/10.1017/S0022112095000462

Karnis, A., Goldsmith, H. L., & Mason, S. G. (1966). The flow of suspensions through tubes V. Inertial effects. *Canadian Society for Chemical Engineering, 44*(4), 181–193. https://doi.org/10.1002/cjce.5450440401

Kloss, C., Goniva, C., Hager, A., Amberger, S., & Pirker, S. (2012). Models, algorithms and validation for opensource DEM and CFD–DEM. *Progress in Computational Fluid Dynamics, an International Journal, 12*, 140–152. https://doi.org/10.1504/PCFD.2012.047457

Kovács, K. A., & Balla, E. (2025). Quantitative comparison of vortex identification methods in three-dimensional fluid flow around bluff bodies. *International Journal of Heat and Fluid Flow, 113*, Article 109773. https://doi.org/10.1016/j.ijheatfluidflow.2025.109773

Liu, W., & Wu, C. Y. (2021). Inertial migration of a neutrally buoyant circular particle in a planar Poiseuille flow with thermal fluids. *Physics of Fluids, 33*, Article 063315. https://doi.org/10.1063/5.0051024

Luo, W., Parteli, E. J. R., Pöschel, T., & Fan, F. (2026). Inertial migration regimes of a neutrally buoyant sphere in pipe Poiseuille flow. *Journal of Fluid Mechanics, 1029*, A53. https://doi.org/10.1017/jfm.2026.11211

Matas, J. P., Morris, J. F., & Guazzelli, É. (2004). Inertial migration of rigid spherical particles in Poiseuille flow. *Journal of Fluid Mechanics, 515*, 171–195. https://doi.org/10.1017/S0022112004000254

Matas, J. P., Morris, J. F., & Guazzelli, É. (2009). Lateral force on a rigid sphere in large-inertia laminar pipe flow. *Journal of Fluid Mechanics, 621*, 59–67. https://doi.org/10.1017/S0022112008004977

Moerland, C. P., Van Ijzendoorn, L. J., & Prins, M. W. J. (2019). Rotating magnetic particles for lab-on-chip applications–A comprehensive review. *Lab on a Chip, 19*(6), 919–933. https://doi.org/10.1039/C8LC01323C

Morita, Y., Itano, T., & Sugihara-Seki, M. (2017). Equilibrium radial positions of neutrally buoyant spherical particles over the circular cross-section in Poiseuille flow. *Journal of Fluid Mechanics, 813*, 750–767. https://doi.org/10.1017/jfm.2016.881

National Research Council. (1928). *International critical tables of numerical data, physics, chemistry and technology, 3*. McGraw-Hill.

National Research Council. (1929). *International critical tables of numerical data, physics, chemistry and technology, 5*. McGraw-Hill.

Oliver, D. R. (1962). Influence of particle rotation on radial migration in the Poiseuille flow of suspensions. *Nature, 194*, 1269–1271. https://doi.org/10.1038/1941269b0

Prohm, C., Zöller, N., & Stark, H. (2014). Controlling inertial focussing using rotational motion. *The European Physical Journal E, 37*, Article 36. https://doi.org/10.1140/epje/i2014-14036-y

Ren, W. L., Zhang, X. H., Zhang, Y., & Lu, X. B. (2023). Investigation of motion characteristics of coarse particles in hydraulic collection. *Physics of Fluids, 35*, Article 043322. https://doi.org/10.1063/5.0142221

Riccardi, M., & Martin, O. J. F. (2023). Electromagnetic forces and torques: From dielectrophoresis to optical tweezers. *Chemical Reviews, 123*(4), 1680–1711. https://doi.org/10.1021/acs.chemrev.2c00576

Saffman, P. G. (1965). The lift on a small sphere in a slow shear flow. *Journal of Fluid Mechanics, 22*, 385–400. https://doi.org/10.1017/S0022112065000824

Schonberg, J. A., & Hinch, E. (1989). Inertial migration of a sphere in Poiseuille flow. *Journal of Fluid Mechanics, 203*, 517–524. https://doi.org/10.1017/S0022112089001564

Takemura, F., & Magnaudet, J. (2003). The transverse force on clean and contaminated bubbles rising near a vertical wall at moderate Reynolds number. *Journal of Fluid Mechanics, 495*, 235–253. https://doi.org/10.1017/S0022112003006232

Xia, Y., Xiong, H., Yu, Z., & Zhu, C. (2020). Effects of the collision model in interface-resolved simulations of particle-laden turbulent channel flows. *Physics of Fluids, 32*, Article 103303. https://doi.org/10.1063/5.0020995

Zeng, L., Balachandar, S., & Fischer, P. (2005). Wall-induced forces on a rigid sphere at finite Reynolds number. *Journal of Fluid Mechanics, 536*, 1–25. https://doi.org/10.1017/S0022112005004738

Zhang, S., Wang, Y., Onck, P., & den Toonder, J. (2020). A concise review of microfluidic particle manipulation methods. *Microfluidics and Nanofluidics, 24*, Article 24. https://doi.org/10.1007/s10404-020-2328-5

Zhou, J., & Papautsky, I. (2020). Viscoelastic microfluidics: Progress and challenges. *Microsystems & Nanoengineering, 6*, Article 113. https://doi.org/10.1038/s41378-020-00218-x